Editors' Suggestion

Tractable T-matrix model for reaction processes in muon-catalyzed fusion $(dt\mu)_{J=v=0} \rightarrow \alpha + n + \mu + 17.6$ MeV or $(\alpha\mu)_{nl} + n + 17.6$ MeV

Qian Wu [1,2,*] and Masayasu Kamimura [3,†]

[1] *School of Physics, Nanjing University, Nanjing 21000, China*

[2] *Institute of Modern Physics, Chinese Academy of Sciences, Lanzhou 730000, China*

[3] *Meson Science Laboratory, RIKEN Nishina Center, RIKEN, Wako 351-0198, Japan*

(Received 30 January 2024; accepted 10 April 2024; published 31 May 2024)

Reaction processes in muon catalyzed fusion (μCF), $(dt\mu)_{J=v=0} \rightarrow \alpha + n + \mu + 17.6$ MeV or $(\alpha\mu)_{nl} + n + 17.6$ MeV in a deuterium-tritium (D-T) mixture were comprehensively studied by Kamimura, Kino, and Yamashita [Phys. Rev. C **107**, 034607 (2023)] by solving the $dt\mu$-$\alpha n\mu$ coupled channel (CC) Schrödinger equation under a boundary condition where the muonic molecule $(dt\mu)_{J=v=0}$ was set as the initial state and the outgoing wave was in the $\alpha n\mu$ channel. We approximate this CC framework and propose a considerably more tractable model using the T-matrix method based on the Lippmann-Schwinger equation. Nuclear interactions adopted in the T-matrix model are determined by reproducing the cross section of the reaction $d + t \rightarrow \alpha + n + 17.6$ MeV at low energies. The cross section of the strong-coupling rearrangement reaction is presented in a simple closed form based on our new model. This T-matrix model has reproduced most of the calculated results on the above μCF reaction reported by Kamimura *et al.* (2023) and is applicable to other μCF systems such as $(dd\mu)$, $(tt\mu)$, $(dt\mu)^*$, $(dd\mu)^*$.

DOI: 10.1103/PhysRevC.109.054625

I. INTRODUCTION

To ensure that nuclear fusion occurs within nuclear distance (a few fms) the Coulomb barrier between two nuclei must be overcome, which typically requires very high temperatures. At low temperatures, negative muons injected into a mixture of deuterium (D) and tritium (T) can catalyze the fusion reaction

$$d + t \rightarrow \alpha + n + 17.6 \text{ MeV}, \tag{1.1}$$

which is energetically the most effective nuclear fusion reaction. Following the catalyzed reaction, free muons can facilitate another fusion reaction taking the well-known cycle illustrated in Fig. 1. This cyclic reaction is called muon catalyzed fusion (μCF). The fusion of the muonic molecule $dt\mu$ has attracted more attention compared to that of molecules such as $dd\mu$, $tt\mu$ from the perspective of utilization as a future energy source. The history of μCF since 1947 has been reviewed in Refs. [1–4]. The present status of the study of $dt\mu$ fusion is briefly summarized in Ref. [5].

Recently, the μCF has regained considerable attention owing to experimental and theoretical developments (i) in the production of energy by μCF using the high-temperature *gas* target of a D/T mixture with high thermal efficiency and (ii) in an ultraslow negative muon beam by utilizing μCF for various applications including scanning negative muon microscope and an injection source for the muon collider. This is explained in detail in the Introduction of Ref. [5].

The study of Ref. [5] performed a comprehensive examination of the following $dt\mu$ fusion reaction:

$$(dt\mu)_{J=v=0} \rightarrow \alpha + n + \mu + 17.6 \text{ MeV} \tag{1.2a}$$

$$\searrow (\alpha\mu)_{nl} + n + 17.6 \text{ MeV}. \tag{1.2b}$$

For the first time, this study solved a coupled-channel (CC) Schrödinger equation for the reaction (1.2) using the appropriate boundary conditions where $(dt\mu)_{J=v=0}$ was set as the initial state and the outgoing wave was expressed in the $\alpha n\mu$ channel. All interactions were selected such that the low-energy cross sections of the reaction (1.1) were reproduced using the CC calculations for the reaction. They calculated the fusion rate of the $(dt\mu)_{J=v=0}$ molecule, energy (momentum) spectra of the muon emitted by μCF, and α-μ sticking probability [5].

As investigated in Ref. [6], the $dd\mu$ and $tt\mu$ fusions play important roles for the new kinematics of the μCF cycle in case of high temperature D-T mixtures. Although the $dd\mu$ fusion is known to be considerably weaker than $dt\mu$ fusion, the former should be studied more precisely because the $dd\mu$ experiment is an important preliminary experiment of $dt\mu$, which has a difficulty in the tritium treatment. Although a study on reaction processes in the $dd\mu$ and $tt\mu$ fusion is underway [7] using the same CC method of Ref. [5], solving the CC equations for the reactions expressed as Eq. (1.2) is difficult. Therefore, creating a starting point from the CC method [5], such as an approximation method that simulates their results more easily would be beneficial.

*qwu@nju.edu.cn

†mkamimura@a.riken.jp

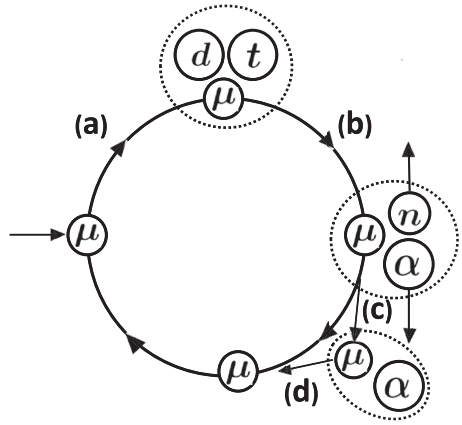

FIG. 1. Schematic diagram of the μCF cycle by a muon injected into the D/T mixture. (a) Formation of $dt\mu$ molecule, (b) fusion reaction, (c) α-μ initial sticking, and (d) muon reactivation. This illustration is taken from Ref. [5].

The purpose of the present paper is to propose considerably more tractable T-matrix model than the aforementioned CC model of Ref. [5]. Instead of directly solving the CC Schrödinger equations for the reactions (1.1) and (1.2), we approximate the T matrix based on the Lippmann-Schwinger equation [8] that is equivalent to the Schrödinger equation. Nuclear interactions are selected to reproduce the cross section of reaction (1.1) at the center-of-mass (c.m.) energy $\approx$1–300 keV. The total angular momentum I and parity of the scattering states is known to be $I^\pi = 3/2^+$. In the following, we explain the scenario of our model in Steps (i)–(v).

Step (i). First, we reproduce the cross section of low-energy reaction (1.1) by using the d-t optical-potential model adopted in Refs. [9]. Absorption cross section is regarded as the cross section of reaction (1.1) because no other open channels exist at these energies than the d-t and α-n channels. The d-t scattering wave function is denoted as $\Phi^{(\mathrm{opt})}_{dt,\frac{3}{2}M}$ (Sec. II A).

Step (ii). We diagonalize the $dt\mu$ Hamiltonian composed of the Coulomb potentials and d-t optical potential to obtain the complex eigenenergy $(E_\mathrm{R} + iE_\mathrm{I})$ and wave function $\Phi_{J=v=0}(dt\mu)$ of the ground state of $(dt\mu)$ molecule. The fusion rate (decay rate) of the molecule is expressed as $-2E_\mathrm{I}/\hbar$ (Sec. II B). Here, we introduce $\Phi^{(J=v=0)}_{\frac{3}{2}M}(dt\mu)$ as the product of $\Phi_{J=v=0}(dt\mu)$ and the d-t spin function $\chi_{\frac{3}{2}M}(dt)$.

Step (iii). The cross section of reaction (1.1) can also be expressed by the exact T matrix introduced in Eq. (4.1) of Ref. [5], where $\Psi^{(+)}_\alpha$ denotes the exact solution of the CC wave function for the reaction (1.1) and V_β stands for a coupling potential $V_{dt,\alpha n}$ between the d-t and α-n channels. In our model, we replace the exact $\Psi^{(+)}_\alpha$ with the d-t wave function $\Phi^{(\mathrm{opt})}_{dt,\frac{3}{2}M}$ obtained in Step (i). $\Phi^{(\mathrm{opt})}_{dt,\frac{3}{2}M}$ is considered to include the effects of the outgoing α-n channel using the imaginary part of the d-t potential. The coupling potential $V_{dt,\alpha n}$ is determined by reproducing the cross section of reaction (1.1). Notably, the cross section of a strong coupling rearrangement reaction as shown in Eq. (1.1) is expressed, based on our model, in a simple closed form that can successfully reproduce the observed data at low energies (Sec. III). This coupling potential $V_{dt,\alpha n}$ is used in Steps (iv) and (v).

Step (iv). In the work of Ref. [5], the T matrix (4.1) was used to study the three-body fusion reaction (1.2) in the manner of Eqs. (5.2)–(5.7) with outgoing waves in the $(\alpha\mu)$-n channel. There, the exact $\Psi^{(+)}_\alpha$ in the T matrix was replaced with the three-body CC wave function $\Psi^{(+)}_{\frac{3}{2}M}$ of Eq. (3.3) [5]. In our model, the exact $\Psi^{(+)}_\alpha$ is replaced with the wave function $\Phi^{(J=v=0)}_{\frac{3}{2}M}(dt\mu)$ of the $dt\mu$ molecule obtained in Step (ii). Further, the α-μ sticking probability is derived using the fusion rates to the α-μ continuum states and those to the α-μ bound states.

Step (v). We make another calculation of the fusion rate of reaction (1.2) using T matrix (4.1) in Ref. [5] with outgoing waves in the (αn)-μ channel. The exact $\Psi^{(+)}_\alpha$ of Eq. (3.3) in Ref. [5] is again replaced with $\Phi^{(J=v=0)}_{\frac{3}{2}M}(dt\mu)$ as in iv). We further calculate the momentum and energy spectrum of the muons emitted by μCF.

We shall examine 20 sets of the parameters for the nuclear interactions and show that the results do not significantly depend on the choice of the parameter sets as long as the reaction (1.1) is explained by using them. We shall report that most of the results obtained in Ref. [5] are well reproduced by the present model.

This paper is organized as follows. In Sec. II, using the optical-potential model, we calculate the cross section of reaction (1.1) and fusion rate of the $(dt\mu)_{J=v=0}$ molecule. In Sec. III, the coupling potential between d-t and α-n channels is determined using the T-matrix method. In Sec. IV, we calculate the α-μ sticking probability and the fusion rate of $(dt\mu)_{J=v=0}$ with the method described in Step (iv). In Sec. V, the spectra of the muons emitted by μCF and the fusion rate of the $(dt\mu)_{J=v=0}$ are calculated using the method in Step (v). The conclusions are presented in Sec. VI.

II. OPTICAL-POTENTIAL MODEL FOR FUSION PROCESSES

A. Fusion cross section

Following Step (i), we first investigate the fusion reaction (1.1) by using the optical-potential model of Ref. [9]. The potential parameters of the nuclear d-t potential are determined by reproducing the cross section of the reaction. The total angular-momentum and parity J^π of the reaction (1.1) at low energies is $I^\pi = 3/2^+$ with S wave and spin 3/2 in the d-t channel while D wave and spin 1/2 in the α-n channel.

We present the d-t scattering wave function $\Phi^{(\mathrm{opt})}_{dt,\frac{3}{2}M}(E,\mathbf{r})$ at the c.m. energy E as

$$\Phi^{(\mathrm{opt})}_{dt,\frac{3}{2}M}(E,\mathbf{r}) = \phi^{(\mathrm{opt})}_{dt,00}(E,\mathbf{r})\,\chi_{\frac{3}{2}M}(dt), \tag{2.1}$$

where $\phi^{(\mathrm{opt})}_{dt,00}(E,\mathbf{r})$ is the spatial part of the S-wave function and $\chi_{\frac{3}{2}M}(dt)$ is the d-t spin 3/2 function. Schrödinger equation for $\phi^{(\mathrm{opt})}_{dt,00}(E,\mathbf{r})$ is presented as

$$(H_{dt} - E)\,\phi^{(\mathrm{opt})}_{dt,00}(E,\mathbf{r}) = 0, \tag{2.2}$$

$$H_{dt} = T_\mathbf{r} + V^{(\mathrm{N})}_{dt}(r) + iW^{(\mathrm{N})}_{dt}(r) + V^{(\mathrm{Coul})}_{dt}(r), \tag{2.3}$$

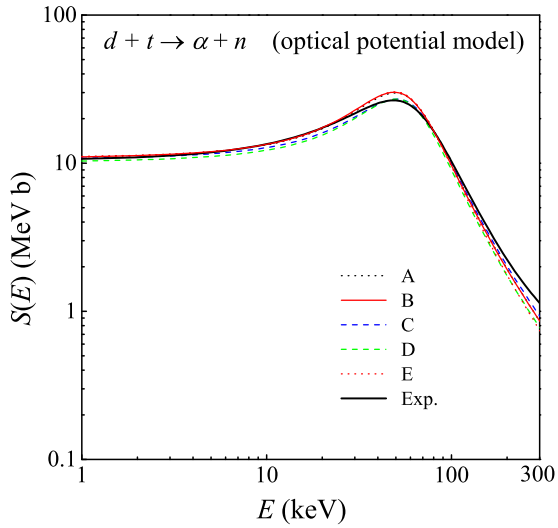

FIG. 2. Calculated S factor $S(E)$ of the reaction $d + t \to \alpha + n + 17.6$ MeV using five different d-t optical potentials A to E listed in Table I. The black solid line (Exp.) is taken from a review paper [10]; it fits the literature data using the function $S(E) = (26 - 0.361E + 248E^2)/1 + [(E - 0.0479)/0.0392]^2$ MeV b (E in MeV).

where the spin-independent d-t optical potential is given by

$$V_{dt}^{(\mathrm{N})}(r) = V_0/\{1 + e^{(r-R_0)/a}\}, \tag{2.4}$$

$$W_{dt}^{(\mathrm{N})}(r) = W_0/\{1 + e^{(r-R_1)/a_1}\}, \tag{2.5}$$

$$V_{dt}^{(\mathrm{Coul})}(r) = \begin{cases} (e^2/(2R_\mathrm{c}))\left(3 - r^2/R_\mathrm{c}^2\right), & r < R_\mathrm{c} \\ e^2/r, & r \geqslant R_\mathrm{c} \end{cases} \tag{2.6}$$

with taking the charge radius $R_\mathrm{c} = R_0$.

In the energy regions shown in Fig. 2, only the α-n channel is open, except for the incoming channel. Therefore, the absorption cross section becomes the cross section of the reaction (1.1) as

$$\sigma_{dt\to\alpha n}(E) = \frac{2I+1}{(2I_d+1)(2I_t+1)}\frac{\pi}{k^2}(1 - |S_J(E)|^2) \tag{2.7}$$

with S-matrix $S_J(E)$. In Eq. (2.7), $I_d = 1$, $I_t = 1/2$, and $k = \sqrt{2\mu_{dt}E}/\hbar$. The astrophysical S factor $S(E)$ is derived from the cross section as

$$\sigma_{dt\to\alpha n}(E) = S(E)\, e^{-2\pi\eta(E)}/E, \tag{2.8}$$

where $\eta(E)$ denotes the Sommerfeld parameter.

Owing to the lack of d-t elastic scattering information for $E \lesssim 300$ keV demonstrating the nuclear-interaction effect, it is impossible to determine a unique d-t optical potential based on the observed S factor in Fig. 2 (black solid line). Therefore, in Ref. [9], five sets of d-t optical potentials, denoted as A–E, were selected to reproduce the observed data. In the present study, the parameter W_0 is changed slightly to improve the agreement with the experimental S factor $S(E)$ for $E \leqslant 10$ keV. The calculated $S(E)$ values with optical potentials A–E are shown in Fig. 2; within the experimental error range [10], the observed $S(E)$ is reproduced well. The potential parameters are listed in Table I.

TABLE I. Five sets (A to E) of the d-t optical-potential parameters.

	V_0 (MeV)	R_0 (fm)	a (fm)	W_0 (MeV)	R_I (fm)	a_I (fm)
A	−58.52	2.5	0.3	−0.30	2.5	0.3
B	−38.01	3.0	0.5	−0.30	3.0	0.5
C	−28.27	3.0	1.0	−0.66	2.0	1.0
D	−16.04	5.0	0.3	−0.22	2.5	0.3
E	−13.19	5.0	1.0	−0.33	3.0	1.0

B. Fusion rate of muonic molecule

Following Step (ii), we calculate the fusion rate of the reaction (1.2) by diagonalizing the $dt\mu$ three body Hamiltonian including the Coulomb force and the d-t nuclear complex potentials determined in the previous subsection. We perform a nonadiabatic three-body calculation of the ground-state wave function of the $dt\mu$ molecule, $\Phi_{J=v=0}(dt\mu)$, using the Gaussian expansion method (GEM) for few-body systems [11–13]:

$$(H_{dt\mu} - E_{00})\,\Phi_{J=v=0}(dt\mu) = 0, \tag{2.9}$$

$$H_{dt\mu} = T_{\mathbf{r}_c} + T_{\mathbf{R}_c} + V^{(\mathrm{C})}(r_1) + V^{(\mathrm{C})}(r_2) + V_{dt}^{(\mathrm{N})}(r_3) + iW_{dt}^{(\mathrm{N})}(r_3) + V_{dt}^{(\mathrm{C})}(r_3). \tag{2.10}$$

$\Phi_{J=v=0}(dt\mu)$ is constructed as the sum of amplitudes of the three rearrangement channels $c = 1$, 2, and 3 as shown in Fig. 3:

$$\Phi_{J=v=0}(dt\mu) = \Phi_0^{(1)}(\mathbf{r}_1, \mathbf{R}_1) + \Phi_0^{(2)}(\mathbf{r}_2, \mathbf{R}_2) + \Phi_0^{(3)}(\mathbf{r}_3, \mathbf{R}_3). \tag{2.11}$$

The amplitude of each channel c is expanded in terms of Gaussian basis functions of the Jacobian coordinates r_c and R_c:

$$\Phi_0^{(c)}(\mathbf{r}_c, \mathbf{R}_c) = \sum_{n_s l_c, N_c L_c} A^{(c)}_{n_c l_c, N_c L_s}\left[\phi_{n_c l_c}(\mathbf{r}_c)\psi_{N_c L_c}(\mathbf{R}_c)\right]_{00}, \tag{2.12}$$

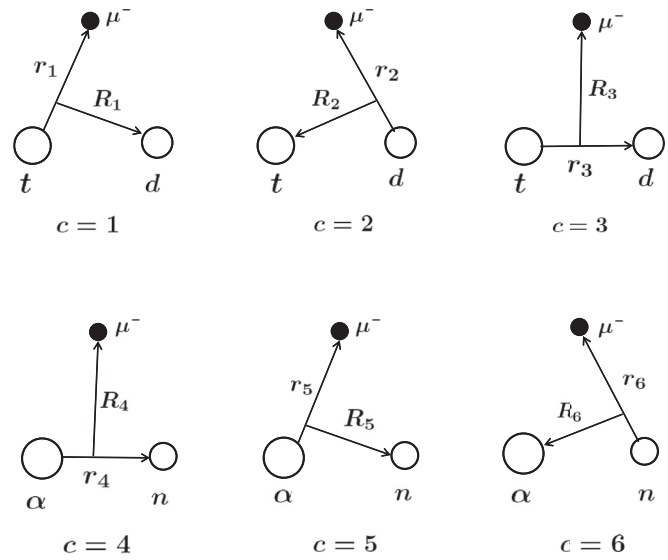

FIG. 3. Three-body Jacobi coordinates used in this study.

TABLE II. Nonlinear variational parameters of the Gaussian basis functions in Eqs. (2.13) and (2.14). $r_1(R_1)$ and $r_{\max}(R_{\max})$ are in units of a_μ where $a_\mu = \hbar^2/m_\mu e^2 = 255.9$ fm, m_μ being the muon mass.

c	l_c	$n_{\max}$	r_1 $[a_\mu]$	$r_{n_{\max}}$ $[a_\mu]$	L_c	$N_{\max}$	R_1 $[a_\mu]$	$R_{N_{\max}}$ $[a_\mu]$
1	0	25	0.1	10	0	15	0.05	10
2	0	25	0.1	10	0	15	0.05	10
3	0	25	0.1	10	0	15	0.05	10
1	1	15	0.2	10	1	15	0.3	15
2	1	15	0.2	10	1	15	0.3	15
3	1	15	0.2	10	1	15	0.3	15
3	0	25	0.001	0.05	0	15	0.05	10

where $c = 1$–3 and

$$\begin{aligned}
&\phi_{nlm}(\mathbf{r}) = \phi_{nl}(r)Y_{lm}(\hat{\mathbf{r}}),\\
&\phi_{nl}(r) = N_{nl}r^l e^{-\nu_n r^2}, \quad (n = 1 - n_{\max}),\\
&\psi_{NLM}(\mathbf{R}) = \psi_{NL}(R)Y_{LM}(\widehat{\mathbf{R}}),\\
&\psi_{NL}(R) = N_{NL}R^L e^{-\lambda_N R^2}, \quad (N = 1 - N_{\max}) \qquad (2.13)
\end{aligned}$$

with normalization constants N_{nl} and N_{NL}. The Gaussian range parameters ν_n and λ_n are chosen in geometric progression:

$$\begin{aligned}
&\nu_n = 1/r_n^2, \quad r_n = r_1 a^{n-1}, \quad (n = 1 - n_{\max}),\\
&\lambda_N = 1/R_N^2, \quad R_N = R_1 A^{N-1}, \quad (N = 1 - N_{\max}). \qquad (2.14)
\end{aligned}$$

Subsequently, the eigenenergy and wave function are obtained using the Rayleigh-Ritz variational method. The advantages of using the GEM basis functions are explained in detail in Sec. III A in Ref. [14].

As the eigenenergy E_{00} is a complex number, we write $E_{00} = E_{00}^{(\mathrm{real})} + iE_{00}^{(\mathrm{imag})}$. We introduce $\varepsilon_{00} = E_{00}^{(\mathrm{real})} - E_{\mathrm{th}}$, with $E_{\mathrm{th}}(= -2711.24$ eV) being the $(t\mu)_{1s} + d$ threshold energy. The diagonalization in the cases of $l_{\max} = 4$ and $l_{\max} = 1$ yield, respectively, $\varepsilon_{00} = -319.14$ eV and -319.12 eV. According to Ref. [5], the digits below 1 eV did not affect the reaction calculation. Thus, we employ $l_{\max} = 1$. The input Gaussian basis is shown in Table II. We took seven lines of Gaussian basis parameters where the final line is effective to the d-t nuclear interaction.

The fusion rate $\lambda_{\mathrm{f}}^{(0)}$ of reaction (1.2) can be derived by $\lambda_{\mathrm{f}}^{(0)} = -2E_{00}^{(\mathrm{imag})}/\hbar$ and is given as $\lambda_{\mathrm{f}}^{(0)} = (1.11 \pm 0.04) \times 10^{12}\mathrm{s}^{-1}$ using five sets of the d-t potentials as presented in Table III. It is consistent with the results $1.15 \times 10^{12}\mathrm{s}^{-1}$ obtained in Ref. [5].

TABLE III. Fusion rate of the reaction (1.2) using the five sets (A to E) of the d-t optical-potential parameters in Table I.

	A	B	C	D	E
$\lambda_f^{(0)}(10^{12}\mathrm{s}^{-1})$	1.14	1.15	1.12	1.07	1.07

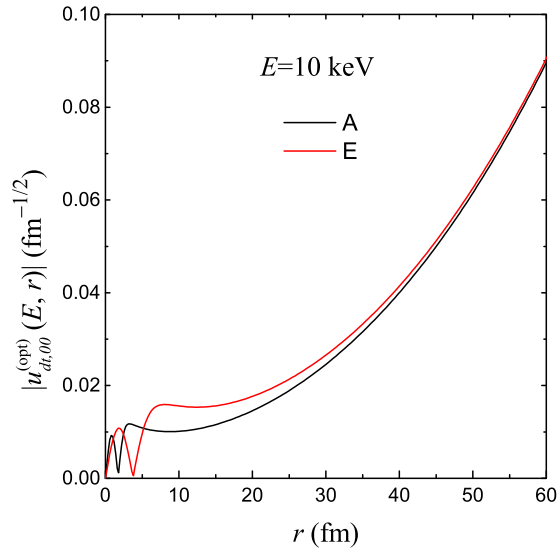

FIG. 4. Absolute value of the d-t radial wave function $u_{dt,00}^{(\mathrm{opt})}(E,r)$ in Eq. (2.15) at $E = 10$ keV with the use of optical potentials A and E in black and red lines, respectively.

Here, we consider why the use of quite different sets of potentials A to E that reproduce the observed S factor can result in almost the same fusion rates of the $dt\mu$ molecule. In Fig. 4, we illustrate the absolute value of the radial wave function $u_{dt,00}^{(\mathrm{opt})}(E,r)$ defined using $\phi_{dt,00}^{(\mathrm{opt})}(E,\mathbf{r})$ in Eq. (2.1) as

$$\phi_{dt,00}^{(\mathrm{opt})}(E,\mathbf{r}) = \frac{1}{r}u_{dt,00}^{(\mathrm{opt})}(E,r)Y_{00}(\hat{\mathbf{r}}) \qquad (2.15)$$

in the case of using the potentials A and E at $E = 10$ keV. The two lines are quite different in the interaction region, but approach each other in the asymptotic region (the case of potentials B–D are between the two lines); similarly for the real and imaginary components of $u_{dt,00}^{(\mathrm{opt})}(E,r)$. This means that all cases result in almost the same absorption cross section (2.7) of the d-t scattering. The same behavior is observed for other energies seen in Fig. 2. In the fusion time of the $dt\mu$ molecule, the d and t approach each other with very low energies[1] passing under the Coulomb barrier and cause the reaction (1.1) with negligible influence from the third particle, the far-away muon. Therefore, the fusion behavior in the asymptotic region exhibits almost no difference among the cases of potentials A to E. It will be shown that this consideration also works in the following sections about various behaviors of the $dt\mu$ fusion in the asymptotic region.

For the sake of the following calculations, we multiply $\Phi_{J=v=0}(dt\mu)$ by the d-t spin function $\chi_{\frac{3}{2}M}(dt)$:

$$\Phi_{\frac{3}{2}M}^{(J=v=0)}(dt\mu) = \Phi_{J=v=0}(dt\mu)\,\chi_{\frac{3}{2}M}(dt), \qquad (2.16)$$

which will be used in Secs. IV and V as the ground-state wave function the $(dt\mu)$ molecule.

[1]Dominant contribution to the fusion rate $\lambda_f^{(0)}$ comes from the resonance tail below $E \approx 10$ keV in Fig. 2, not from the resonance peak. This was presented in Fig. 5 of Ref. [14].

III. T-MATIX MODEL FOR $d + t \to \alpha + n + 17.6$ MeV

In this section, following Step (iii), we propose tractable T-matrix model for the reaction (1.1) to approximate the CC model described in Ref. [5] [cf. Eqs. (2.1)–(2.10)] using the results of the optical-potential model in the previous section.

At low energies, the d-t wave function has the total angular momentum $I = 3/2$ with an S wave in the d-t channel and D wave in the α-n channel. The authors of Ref. [5] solved the following dt-αn CC Schrödinger equation ($Q = 17.6$ MeV) using the coordinates $\mathbf{r}_3$ and $\mathbf{r}_4$ for the d-t and α-n motion, respectively (cf. Fig. 3):

$$\begin{aligned}(H_{dt} - E)\,\Phi_{dt,\,\frac{3}{2}M}(\mathbf{r}_3) &= -V^{(\mathrm{T})}_{dt,\alpha n}(\mathbf{r}_3,\mathbf{r}_4)\,\Phi^{(+)}_{\alpha n,\,\frac{3}{2}M}(\mathbf{r}_4),\\ (H_{\alpha n} - (E+Q))\Phi^{(+)}_{\alpha n,\,\frac{3}{2}M}(\mathbf{r}_4) &= -V^{(\mathrm{T})}_{\alpha n,dt}(\mathbf{r}_4,\mathbf{r}_3)\,\Phi_{dt,\,\frac{3}{2}M}(\mathbf{r}_3)\end{aligned} \tag{3.1}$$

with trivial notations. The channel-coupling potential $V^{(\mathrm{T})}_{\alpha n,dt}$ ($V^{(\mathrm{T})}_{dt,\alpha n}$) is of the tensor type. The reaction cross section is presented as

$$\sigma_{dt\to\alpha n}(E) = \frac{2I+1}{(2I_d+1)(2I_t+1)}\frac{\pi}{k^2}\,|S_2^{(dt,\alpha n)}|^2, \tag{3.2}$$

where the S matrix $S_2^{(dt,\alpha n)}$ appears in the asymptotic form of the outgoing wave, $\Phi^{(+)}_{\alpha n,\,\frac{3}{2}M}$ [5].

According to the Lippmann-Schwinger theory, the cross section is alternatively expressed exactly as follows using the solution $\Phi_{dt,\,\frac{3}{2}M}$ and $\Phi^{(+)}_{\alpha n,\,\frac{3}{2}M}$ of Eq. (3.1) (cf. Sec. IV A of Ref. [5]):

$$\sigma_{dt\to\alpha n}(E) = \frac{v_4}{v_3}\left(\frac{\mu_{r_4}}{2\pi\hbar^2}\right)^2 \sum_{m_s}\int \left|T^{(1)}_{m_s} + T^{(2)}_{m_s}\right|^2 \mathrm{d}\widehat{\mathbf{K}}, \tag{3.3}$$

$$T^{(1)}_{m_s} = \left\langle e^{i\mathbf{K}\cdot\mathbf{r}_4}\,\chi_{\frac{1}{2}m_s}(n)\right|\left. V^{(\mathrm{T})}_{\alpha n,dt}\right|\,\Phi_{dt,\,\frac{3}{2}M}\Big\rangle, \tag{3.4}$$

$$T^{(2)}_{m_s} = \left\langle e^{i\mathbf{K}\cdot\mathbf{r}_4}\,\chi_{\frac{1}{2}m_s}(n)\right|\left. V_{\alpha n}\right|\,\Phi^{(+)}_{\alpha n,\,\frac{3}{2}M}\Big\rangle, \tag{3.5}$$

where $\chi_{\frac{1}{2}m_s}(n)$ is the neutron spin function, $V_{\alpha n}$ is the α-n potential, v_3 (v_4) is the velocity of the d-t (α-n) relative motion along $\mathbf{r}_3$ ($\mathbf{r}_4$), μ_{r_4} is the reduced mass associated with $\mathbf{r}_4$, and $\mathbf{K}$ is the wave number vector.

The coupling potential $V^{(\mathrm{T})}_{\alpha n,dt}$ between the αn-dt channels are taken in the following form [5]:

$$V^{(\mathrm{T})}_{\alpha n,dt}(\mathbf{r}_4,\mathbf{r}_3) = v_0^{(\mathrm{T})} r_{34}^2 e^{-\mu r_{34}^2 - \mu' R_{34}^2}\,[Y_2(\widehat{\mathbf{r}}_{34})\,\mathcal{S}_2(dt,\alpha n)]_{00}, \tag{3.6}$$

where $\mathbf{r}_{34} = \mathbf{r}_3 - \mathbf{r_4}$ and $\mathbf{R}_{34} = \mathbf{r}_3 + \mathbf{r_4}$. In Eq. (3.6), $\mathcal{S}_2(dt,\alpha n)$ is a spin-tensor operator comprising the spins of dt and αn pairs. However, the explicit form of $\mathcal{S}_2(dt,\alpha n)$ needs not to be determined as explained below [cf. Eq. (3.4)].

In our model, we perform another T-matrix calculation for $\sigma_{dt\to\alpha n}(E)$ by using Eq. (3.3) considering the following approximation. We replace $\Phi_{dt,\,\frac{3}{2}M}$ in $T^{(1)}_{m_s}$ with $\Phi^{(\mathrm{opt})}_{dt,\,\frac{3}{2}M}$ in Eq. (2.1) and neglect $T^{(2)}_{m_s}$ because $\Phi^{(\mathrm{opt})}_{dt,\,\frac{3}{2}M}$ does not include the α-n component explicitly. However, $\Phi^{(\mathrm{opt})}_{dt,\,\frac{3}{2}M}$ is considered to reflect the effect of the α-n channel using the imaginary potential $iW^{(\mathrm{N})}_{dt}(r_3)$ in Eq. (2.2). Thus, Eqs. (3.3)–(3.5) are approximated as

$$\sigma^{(\mathrm{our})}_{dt\to\alpha n}(E) = \frac{v_4}{v_3}\left(\frac{\mu_{r_4}}{2\pi\hbar^2}\right)^2 \sum_{m_s}\int \left|T^{(1')}_{m_s}\right|^2 \mathrm{d}\widehat{\mathbf{K}}, \tag{3.7}$$

$$T^{(1')}_{m_s} = \left\langle e^{i\mathbf{K}\cdot\mathbf{r}_4}\,\chi_{\frac{1}{2}m_s}(n)\right|\left. V^{(\mathrm{T})}_{\alpha n,dt}(\mathbf{r}_4,\mathbf{r}_3)\right|\,\Phi^{(\mathrm{opt})}_{dt,\,\frac{3}{2}M}(E,\mathbf{r}_3)\Big\rangle. \tag{3.8}$$

Instead of Eq. (3.6), we employ the following separable nonlocal form:

$$V^{(\mathrm{T})}_{\alpha n,dt}(\mathbf{r}_4,\mathbf{r}_3) = v_0^{(\mathrm{T})} r_4^2\, e^{-\mu_4 r_4^2 - \mu_3 r_3^2}\,[Y_2(\widehat{\mathbf{r}}_4)\,\mathcal{S}_2(dt,\alpha n)]_{00}, \tag{3.9}$$

which is easier to handle than Eq. (3.6). Consequently, the cross section (3.7) can be explicitly expressed as

$$\sigma^{(\mathrm{our})}_{dt\to\alpha n}(E) = \frac{v_4}{v_3}\left(\frac{\mu_{r_4}}{2\pi\hbar^2}\right)^2 \left|\, v_0^{(T)} S_0^{(T)} F_0\, J_2\,\right|^2 \tag{3.10}$$

with

$$F_0 = \int \phi^{(\mathrm{opt})}_{dt,00}(E,\mathbf{r}_3)\, e^{-\mu_3 r_3^2}\,\mathrm{d}\mathbf{r}_3, \tag{3.11}$$

$$\begin{aligned}J_2 &= 4\pi\int j_2(Kr_4)\, r_4^2\, e^{-\mu_4 r_4^2}\, r_4^2\,\mathrm{d}r_4\\ &= \frac{1}{4}\left(\frac{\pi}{\mu_4}\right)^{\frac{3}{2}}\left(\frac{K}{\mu_4}\right)^2 e^{-\frac{\mu_4 K^2}{4}},\end{aligned} \tag{3.12}$$

where $\phi^{(\mathrm{opt})}_{dt,00}(E,\mathbf{r}_3)$ is normalized asymptotically as

$$\phi^{(\mathrm{opt})}_{dt,00}(E,\mathbf{r}_3) \overset{r_3\to\infty}{\longrightarrow} e^{i\sigma_0}\frac{F_0(k,r_3)}{kr_3} + (\text{outgoing wave}) \tag{3.13}$$

with the S-wave Coulomb function $F_0(k,r)$ and phase shift σ_0. $j_2(kr_4)$ is the spherical Bessel function of order 2. In Eq. (3.10), the constant $S_0^{(\mathrm{T})}$ is presented, independently of m_s, as (cf. Eq. (2.12) of Ref. [5])

$$S_0^{(\mathrm{T})} = \frac{1}{\sqrt{10}}\left\langle \chi_{\frac{1}{2}m_s}(\alpha n)\right|\left[\mathcal{S}_2(dt,\alpha n)\,\chi_{\frac{3}{2}}(dt)\right]_{\frac{1}{2}m_s}\Big\rangle. \tag{3.14}$$

Therefore, the explicit form of $S_2(dt,\alpha n)$ needs not to be known, and $v_0^{(\mathrm{T})}S_0^{(\mathrm{T})}$ can be considered as an adjustable parameter for the T-matrix calculations.

We determined the parameter sets for the dt-αn coupling potential $V^{(\mathrm{T})}_{\alpha n,dt}(\mathbf{r}_4,\mathbf{r}_3)$ in Eq. (3.9) so as to reproduce the observed S factor $S(E)$. We employed, in Eq. (3.8), $\Phi^{(\mathrm{opt})}_{dt,\,\frac{3}{2}M}(E,\mathbf{r}_3)$ obtained in Sec. II A using the optical potentials A–E in Table I. The resulting parameters are listed in Table IV. Sets A1–A4 were obtained using the optical potential of Set A, and similarly for others.

In Fig. 5, the calculated $S(E)$ factors using Sets A1–E1 are illustrated. The experimental data are well reproduced with the same quality of fitting as in Fig. 4 by the CC calculation in of Ref. [5]. The use of the other sets yielded a similar agreement. Subsequently, we employ all dt-αn tensor coupling potentials in Secs. IV and V. The cross section of the strong coupling rearrangement reaction (1.1) is expressed in a simple closed form (3.10)–(3.12) that can reproduce observed

TABLE IV. Parameters of the dt-αn coupling potential $V^{(\mathrm{T})}_{\alpha n,dt}(\mathbf{r}_4,\mathbf{r}_3)$ in Eq. (3.9). Sets A1–A4 were determined using the optical potential Set A in Table I; similarly for the others.

Potential set	$v_0^{(\mathrm{T})} S_0^{(\mathrm{T})}$ (MeV fm^{-5})	$\mu_3^{-1/2}$ (fm)	$\mu_4^{-1/2}$ (fm)
Set A1	2.307	1.6	1.6
Set A2	0.138	2.0	5.2
Set A3	0.245	3.2	1.6
Set A4	0.402	2.0	2.8
Set B1	1.001	2.8	1.6
Set B2	0.016	4.0	2.4
Set B3	0.065	3.6	2.0
Set B4	0.003	4.0	5.6
Set C1	0.122	2.4	2.4
Set C2	0.052	1.6	6.4
Set C3	0.029	3.2	4.8
Set C4	0.191	4.4	1.6
Set D1	1.291	3.6	1.6
Set D2	0.151	3.2	2.0
Set D3	0.405	4.4	1.6
Set D4	0.032	4.0	5.6
Set E1	0.054	5.2	2.0
Set E2	0.166	2.0	2.0
Set E3	0.054	4.4	2.8
Set E4	0.019	4.4	5.2

data by tuning the parameters of $V^{(\mathrm{T})}_{\alpha n,dt}(\mathbf{r}_4,\mathbf{r}_3)$. This is a key finding of this study.

Here, we highlight the consistency of our model in terms of its potentials. In the process of tuning the potential parameter sets, we considered the plane wave (D wave) of the α-n relative motion in the T matrix (3.8) where the α-n potential

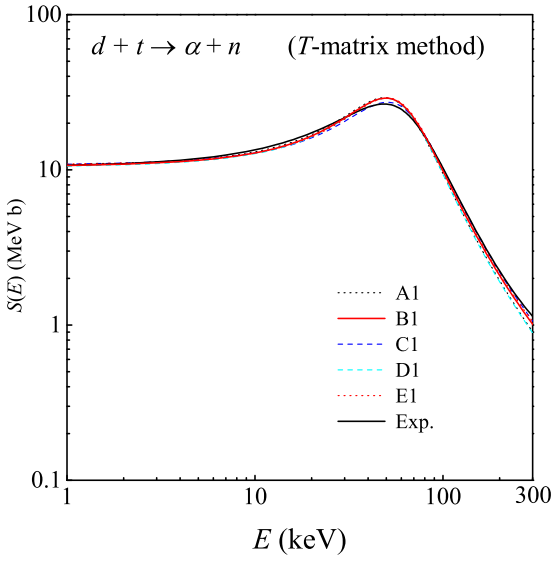

FIG. 5. Calculated S factor $S(E)$ of the reaction $d + t \to \alpha + n + 17.6$ MeV. Five lines A1–E1 denote the cases using the dt-αn coupling potentials with the parameter Sets A1–E1, respectively, in Table IV. The black solid line indicating the experimental data is from a review paper [10].

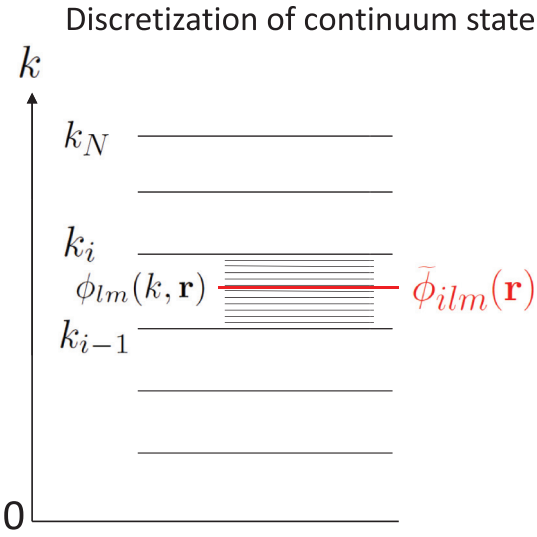

FIG. 6. Schematic illustration of Eq. (4.1) to construct the continuum-discretized wave function $\widetilde{\phi}_{ilm}(\mathbf{r})$ by averaging the continuum wave functions $\phi_{lm}(k,\mathbf{r})$ in each momentum bin $\Delta k_i = k_i - k_{i-1}$.

$V_{\alpha n}(r_4)$ did not appear explicitly. We consider that the effect of the α-n potential is effectively renormalized into the coupling potential $V^{(\mathrm{T})}_{\alpha n,dt}$ which is tuned to reproduce the observed $S(E)$ without $V_{\alpha n}(r_4)$. In Secs. IV and V, we consistently use the same potentials without $V_{\alpha n}(r_4)$ in the T-matrix calculations of the three-body $dt\mu$-$\alpha n\mu$ system. As shown later, most of the results of Ref. [5] are well reproduced by our model.

IV. α-μ STICKING PROBABILITY

After fusion occurs in the $dt\mu$ molecule, the emitted muon can be captured by the α particle or freely emitted, as shown in Eq. (1.2). In this section, according to Step (iv) of the Introduction, we calculate the fusion rate of the reaction (1.2) and the α-μ sticking probability by referring to the T-matrix calculation of those quantities in Sec. IV of Ref. [5] with the outgoing waves in channel $c = 5$ (Fig. 3).

The authors of Ref. [5] solved the CC Schrödinger equation (3.7) for the reaction (1.2) and generated the wave function $\Psi^{(+)}_{\frac{3}{2}M}(E)$ expressed as Eq. (3.3). They constructed the T-matrix elements (5.2)–(5.3) for use in another fusion calculation by substituting their $\Psi^{(+)}_{\frac{3}{2}M}(E)$ into the exact wave function $\Psi^{(+)}_{\alpha}(E_\alpha)$ in the definition of T matrix (4.1) in Ref. [5].

Because the functions $\phi_\beta(\xi_\beta)$ in the outgoing channel β in the T matrix are orthonormalized functions of discrete states, they discretized and orthonormalized the α-μ wave function of the k-continuum state, for example, $\phi_{lm}(k,\mathbf{r}_5)$, to generate $\widetilde{\phi}_{ilm}(\mathbf{r}_5)$ and energy $\widetilde{\varepsilon}_i$. This discretization was performed by employing the procedure (Fig. 6)

$$\widetilde{\phi}_{ilm}(\mathbf{r}_5) = \frac{1}{\sqrt{\Delta k_i}} \int_{k_{i-1}}^{k_i} \phi_{lm}(k,\mathbf{r}_5)\, dk, \quad i = 1 - N, \tag{4.1}$$

$$\widetilde{\varepsilon}_i = \frac{\hbar^2}{2\mu_{r_5}} \widetilde{k}_i^2, \qquad \widetilde{k}_i^2 = \left(\frac{k_i + k_{i-1}}{2}\right)^2 + \frac{\Delta k_i^2}{12}. \tag{4.2}$$

This has often been used in the continuum-discretized coupled-channels (CDCC) method for studying the projectile-breakup reactions (for example, see review papers [15–17]). On the other hand, $\phi_{nlm}(\mathbf{r}_5)$ stands for the bound states $(\alpha\mu)_{nlm}$. Then, it can be said that Ref. [5] investigated the reaction

$$(dt\mu)_{J=v=0} \to (\alpha\mu)_{il} + n + 17.6\,\mathrm{MeV} \quad (4.3)$$

$$\searrow (\alpha\mu)_{nl} + n + 17.6\,\mathrm{MeV}, \quad (4.4)$$

considering a precise discretization of the α-μ continuum.

In our model, we replace $\Psi^{(+)}_{\frac{3}{2}M}(E)$ with $\Phi^{(J=v=0)}_{\frac{3}{2}M}(dt\mu)$ in the T-matrix elements (5.2)–(5.3) in Ref. [5]. This is a key point of the proposed model. $\Phi^{(J=v=0)}_{\frac{3}{2}M}(dt\mu)$ is the ground-state wave function of the $(dt\mu)$ molecule with the total angular momentum spin 3/2 and was obtained in Eqs. (2.9) and (2.15) with the d-t optical potential. As $\Phi^{(J=v=0)}_{\frac{3}{2}M}(dt\mu)$ does not explicitly include the $\alpha n\mu$ amplitude, the third lines of Eqs. (5.2) and (5.3) in Ref. [5] were excluded. $\mathring{\Psi}^{(\mathrm{C})}_{\frac{3}{2}M}(dt\mu) + \Psi^{(\mathrm{N})}_{\frac{3}{2}M}(dt\mu)$ that is the dominant component of $\Psi^{(+)}_{\frac{3}{2}M}(E)$ is replaced with $\Phi^{(J=v=0)}_{\frac{3}{2}M}(dt\mu)$. Consequently, we obtain our T-matrix elements with the outgoing wave functions in channel $c = 5$:

$$\widetilde{T}^{(5)}_{il,mm_s} = \left\langle e^{i\widetilde{\mathbf{K}}_i\cdot\mathbf{R}_5}\,\widetilde{\phi}_{ilm}(\mathbf{r}_5)\chi_{\frac{1}{2}m_s}(n)\right| V^{(\mathrm{T})}_{\alpha n,dt}\left|\,\Phi^{(J=v=0)}_{\frac{3}{2}M}(dt\mu)\right\rangle \quad (4.5)$$

for the transition to discretized states $(\alpha\mu)_{ilm}$, and

$$T^{(5)}_{nl,mm_s} = \left\langle e^{i\mathbf{K}_n\cdot\mathbf{R}_5}\,\phi_{nlm}(\mathbf{r}_5)\chi_{\frac{1}{2}m_s}(n)\right| V^{(\mathrm{T})}_{\alpha n,dt}\left|\,\Phi^{(J=v=0)}_{\frac{3}{2}M}(dt\mu)\right\rangle \quad (4.6)$$

for the transition to bound states $(\alpha\mu)_{nlm}$. Here, we take $\mathbf{R}_4 = \mathbf{R}_3$ [5] (cf. Fig. 3). The $(\alpha\mu)$-n plane waves along $\mathbf{R}_5$ are denoted by $e^{i\widetilde{\mathbf{K}}_i\cdot\mathbf{R}_5}$ and $e^{i\mathbf{K}_n\cdot\mathbf{R}_5}$ in which the momentum $\widetilde{K}_i$ and K_n are derived from energy conservation as follows (cf. Fig. 2 and Sec. V of Ref. [5]):

$$\widetilde{E}_i + \widetilde{\varepsilon}_i = E_{00} + Q, \quad \widetilde{E}_i = \frac{\hbar^2}{2\mu_{R_5}}\widetilde{K}_i^2, \quad (4.7)$$

$$E_n + \varepsilon_n = E_{00} + Q, \quad E_n = \frac{\hbar^2}{2\mu_{R_5}}K_n^2, \quad (4.8)$$

where $\widetilde{\varepsilon}_i$ (ε_n) is the energy of $\widetilde{\phi}_{ilm}(\mathbf{r}_5)$ $[\phi_{nlm}(\mathbf{r}_5)]$ and $E_{00} \simeq 3.030$ keV which is negligible in the present scattering problem compared with $Q = 17.6$ MeV.

For the above discretization of the α-μ continuum states $\phi_{lm}(k, \mathbf{r}_5)$, we considered $N = 200$ for $l = 0$ to 25, and maximum momentum $\hbar k_N = 10\mathrm{MeV}/c$ $(\widetilde{\varepsilon}_N = 487$ keV) with the constant Δk_i, which is the same as those used in Ref. [5].

Reaction rates of the reactions (4.3) and (4.4) are expressed as follows:

$$r_{nl} = v_{nl}\left(\frac{\mu_{R_5}}{2\pi\hbar^2}\right)^2 \times \sum_{m,m_s}\int \left|T^{(5)}_{nl,mm_s}\right|^2 \mathrm{d}\widehat{\mathbf{K}}_n, \quad (4.9)$$

$$\widetilde{r}_{il} = v_{il}\left(\frac{\mu_{R_5}}{2\pi\hbar^2}\right)^2 \times \sum_{m,m_s}\int \left|\widetilde{T}^{(5)}_{il,mm_s}\right|^2 \mathrm{d}\widehat{\widetilde{\mathbf{K}}}_i, \quad (4.10)$$

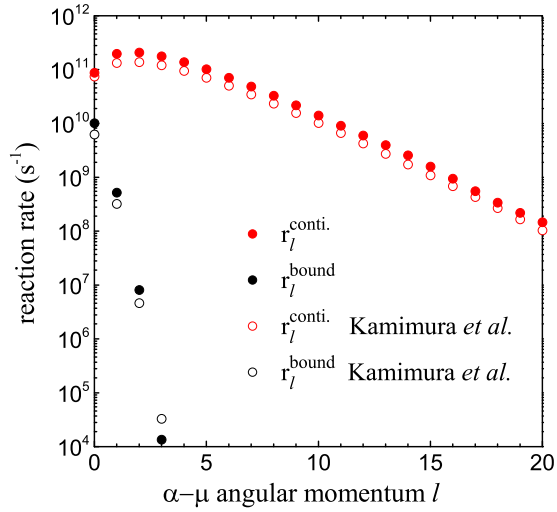

FIG. 7. Calculated reaction rate r_l^{bound} (black closed circle) for the bound state and r_l^{cont} (red closed circle) for the continuum states with respect to the angular momentum l. The black and red open circles are the results of Kamimura *et al.* in Ref. [5] for comparison. The potential Set B1 is used.

which is derived, respectively, by approximating Eqs. (5.6) and (5.7) in Ref. [5] according to our proposed model. Here, $v_{il} = \hbar\widetilde{K}_i/\mu_{R_5}$ is the velocity of the $(\alpha\mu)_{il}$-n relative motion associated with $\mathbf{R}_5$, and similarly for $v_{nl} = \hbar K_n/\mu_{R_5}$. The sum of the quantum number n for r_{nl} and i for $\widetilde{r}_{il}$ yields the total reaction rate r_l^{bound} for the bound states and r_l^{cont} for the continuum states:

$$r_l^{\mathrm{bound}} = \sum_n r_{nl}, \quad r_l^{\mathrm{cont}} = \sum_{i=1}^{N}\widetilde{r}_{il}. \quad (4.11)$$

In Fig. 7, we show the calculated r_l^{bound} and r_l^{cont} with l up to 20 under the potential Set B1 in Table IV. For comparison, we presented the r_l^{bound} and r_l^{cont} obtained in Ref. [5]. Both results have similar tendency with respect to l.

The total reaction rates to the α-μ bound states and continuum states are defined as follows:

$$\lambda_{\mathrm{f}}^{\mathrm{bound}} = \sum_{l=0}^{5} r_l^{\mathrm{bound}}, \quad \lambda_{\mathrm{f}}^{\mathrm{cont.}} = \sum_{l=0}^{20} r_l^{\mathrm{cont.}}. \quad (4.12)$$

Consequently, their sum

$$\lambda_{\mathrm{f}}^{(5)} = \lambda_{\mathrm{f}}^{\mathrm{bound}} + \lambda_{\mathrm{f}}^{\mathrm{cont.}} \quad (4.13)$$

is the fusion rate of the $(dt\mu)_{J=v=0}$ molecule calculated on channel $c = 5$.

Table V lists the fusion rates $\lambda_{\mathrm{f}}^{(5)}$ for all 20 different potential Sets in Table IV. All the fusion rates $\lambda_{\mathrm{f}}^{(5)}$ are within a small range of 1.1–$1.2 \times 10^{12}\mathrm{s}^{-1}$. This proves that the choice of the potentials does not influence the fusion rate significantly. This fusion rate is consistent with $\lambda_{\mathrm{f}}^{(0)}$, which was derived in Sec. II B from the imaginary part of the complex eigenenergy of the $(dt\mu)_{J=v=0}$ molecule. Notably, in the proposed model, the fusion rates $\lambda_{\mathrm{f}}^{(5)}$ have been calculated based on the amplitude of the outgoing $\alpha n\mu$ wave.

TABLE V. Fusion rates $\lambda_{\rm f}^{(5)}$ calculated on the channel $c = 5$ with Eq. (4.13). ω_S^0 is the α-μ sticking probability calculated with Eq. (4.14). See Table IV for the potential sets. Another type of the fusion rate $\lambda_{\rm f}^{(4)}$ is discussed in Sec. V on the channel $c = 4$. $\lambda_{\rm f}^{(5)} = (1.15 \pm 0.05) \times 10^{12}{\rm s}^{-1}$ and $\lambda_{\rm f}^{(4)} = (1.15 \pm 0.04) \times 10^{12}{\rm s}^{-1}$, on average.

Potential set	$\lambda^{(5)}$ (10^{12} s^{-1})	ω_S^0 (%)	$\lambda^{(4)}$ (10^{12} s^{-1})
Set A1	1.12	0.942	1.11
Set A2	1.15	0.943	1.15
Set A3	1.11	0.942	1.11
Set A4	1.13	0.944	1.12
Set B1	1.14	0.942	1.13
Set B2	1.14	0.940	1.12
Set B3	1.13	0.940	1.12
Set B4	1.14	0.939	1.15
Set C1	1.14	0.928	1.14
Set C2	1.18	0.931	1.19
Set C3	1.18	0.945	1.18
Set C4	1.20	0.936	1.19
Set D1	1.13	0.943	1.13
Set D2	1.13	0.941	1.14
Set D3	1.15	0.937	1.13
Set D4	1.17	0.930	1.18
Set E1	1.16	0.935	1.15
Set E2	1.15	0.933	1.14
Set E3	1.16	0.938	1.15
Set E4	1.17	0.937	1.17

The initial α-μ sticking probability ω_S^0 is the probability of the muon being captured by an α particle after the fusion happens. This is expressed by the following formula in the same manner as in Eq. (5.3) in Ref. [5]:

$$\omega_S^0 = \frac{\lambda_{\rm f}^{\rm bound}}{\lambda_{\rm f}^{\rm bound} + \lambda_{\rm f}^{\rm cont.}}. \tag{4.14}$$

The second column of Table V presents the initial sticking probabilities ω_s^0 for different potential sets. The $\omega_s^0 (= 0.938 \pm 0.07\%)$ are consistent and are close to the results (0.91%–0.93%) obtained by using optical-potential models [9,18] and by the R-matrix methods [19–24] considering the d-t nuclear interaction; note that our calculation is based on the *absolute* values of $\lambda_{\rm f}^{\rm bound}$ and $\lambda_{\rm f}^{\rm cont.}$.

However, the values of ω_s^0 in Table V are ≈9% larger than $\omega_s^0 (= 0.857\%)$ given by Ref. [5] in which the coupling to the $\alpha n\mu$ channel is included explicitly. This may be attributed to the following reason. In the CC work [5], strong coupling between the $\alpha n\mu$ outgoing amplitude $\Psi^{(+)}_{\frac{3}{2}M}(\alpha n\mu)$ and the nuclear $dt\mu$ amplitude $\Psi^{(\rm N)}_{\frac{3}{2}M}(dt\mu)$ is expected to enhance the contribution of the transition to the α-μ continuum states in Eqs. (5.2)–(5.3) of Ref. [5] more than that to the α-μ bound states, which enhances the $\lambda_{\rm f}^{\rm cont.}$, and then reduces ω_S^0. However, the present model does not exhibit such a CC effect.

V. MOMENTUM AND ENERGY SPECTRA OF MUON EMITTED BY μCF

In this section, according to Step (v), we calculate the momentum and energy spectra of the muons emitted by reaction (1.2) and derive another type of fusion rate of the $(dt\mu)_{J=v=0}$ molecule. We perform a T-matrix calculation by referring to Sec. VI of Ref. [5] with (αn)-μ outgoing waves in channel $c = 4$ (Fig. 3). We discretize and orthonormalize the wave functions of the α-n continuum states; for example, $\phi_{lm}(k, \mathbf{r}_4)$ with $l = 2$, generating $\widetilde{\phi}_{ilm}(\mathbf{r}_4)$ in the same manner as described in Sec. IV.

We begin with the T matrix expressed as Eq. (6.2) in Ref. [5], where $\Psi^{(+)}_{\frac{3}{2}M}(E)$ is the total wave function obtained using the CC Schrödinger equation (3.7) in Ref. [5]. In the proposed model, we replace $\Psi^{(+)}_{\frac{3}{2}M}(E)$ with $\Phi^{(J=v=0)}_{\frac{3}{2}M}(dt\mu)$ which is the ground-state wave function of the $(dt\mu)$ molecule obtained from Eqs. (2.9) and (2.15) including the d-t optical potential. This is the same key point of our model as mentioned in Sec. IV. Thus, in the three T-matrix elements in Eq. (6.2) of Ref. [5], we exclude the third line because the wave function $\Phi^{(J=v=0)}_{\frac{3}{2}M}(dt\mu)$ does not have an $\alpha n\mu$ scattering amplitude, and replace $\mathring{\Psi}^{(\rm C)}_{\frac{3}{2}M}(dt\mu) + \Psi^{(\rm N)}_{\frac{3}{2}M}(dt\mu)$ with $\Phi^{(J=v=0)}_{\frac{3}{2}M}(dt\mu)$.

We obtain T-matrix elements as follows [cf. Eq. (4.5)]:

$$T^{(4)}_{il,mm_s} = \left\langle e^{i\widetilde{\mathbf{K}}_i\cdot\mathbf{R}_4}\,\widetilde{\phi}_{ilm}(\mathbf{r}_4)\,\chi_{\frac{1}{2}m_s}(n)\middle|\, V^{(\rm T)}_{\alpha n,dt}\,\middle|\,\Phi^{(J=v=0)}_{\frac{3}{2}M}(dt\mu)\right\rangle. \tag{5.1}$$

The outgoing wave is located in channel $c = 4$ and composed of the plane wave $e^{i\widetilde{\mathbf{K}}_i\cdot\mathbf{R}_4}$ and discretized orthonormalized α-n continuum states $\widetilde{\phi}_{ilm}(\mathbf{r}_4)$, which is constructed in the same manner as that in Eq. (4.1) in Sec. IV.

$$\widetilde{\phi}_{ilm}(\mathbf{r}_4) = \frac{1}{\sqrt{\Delta k_i}}\int_{k_{i-1}}^{k_i}\phi_{lm}(k, \mathbf{r}_4)\,dk, \quad (i = 1 - N). \tag{5.2}$$

The average energy $\widetilde{\varepsilon}_i$ and momentum $\widetilde{k}_i$ of $\widetilde{\phi}_{ilm}(\mathbf{r_4})$ are given, similarly to Eq. (4.2). Therefore, the momentum $\widetilde{K}_i$ of the plane wave $e^{i\widetilde{\mathbf{K}}_i\cdot\mathbf{R}_4}$ is derived from the following energy conservation ($Q = 17.6$ MeV):

$$\widetilde{E}_i + \widetilde{\varepsilon}_i = E_{00} + Q, \quad \widetilde{E}_i = \frac{\hbar^2}{2\mu_{R_4}}\widetilde{K}_i^2. \tag{5.3}$$

A new problem in Sec. V is that we aim to generate the set $\{\widetilde{K}_i; i = 1 - N\}$ with equal intervals and obtain the momentum spectrum as a smooth function of K to determine its peak easily. Figure 8 illustrates the manner in which k space is discretized. Following Ref. [5], we first assume the maximum value K_N of K space $[K_0, K_N]$ with $K_0 = 0$ at the left side of the figure. We then divide the K space into N bins $(K_i, i = 0 - N)$ with equal intervals ΔK. Correspondingly, we divide the k space $[k_N, k_0]$ on the right side of the figure to N bins $(k_i, i = 0 - N)$ with the energy conservation kept as

$$E_i + \varepsilon_i = E_{00} + Q, \quad E_i = \frac{\hbar^2}{2\mu_{R_4}}K_i^2, \quad \varepsilon_i = \frac{\hbar^2}{2\mu_{r_4}}k_i^2, \tag{5.4}$$

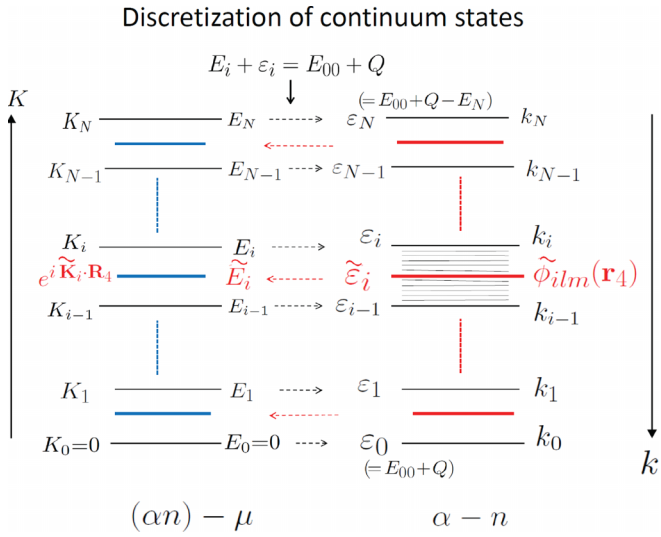

FIG. 8. Schematic illustration for discretization of the momentum space $[K_0, K_N]$ of the (αn)-μ relative motion along $\mathbf{R}_4$ (left half) and that of the α-n relative motion $[k_N, k_0]$ along $\mathbf{r}_4$ (right half) while maintaining $E_i + \varepsilon_i = E_{00} + Q$. The resulting discretized α-n continuum states $\widetilde{\phi}_{ilm}(\mathbf{r}_4)(i = 1 - N)$ are indicated by the red lines. The associated muon plane waves $e^{i\widetilde{\mathbf{K}}_i\cdot\mathbf{R}_4}$ are indicated by the blue lines in the left half. This illustration is taken from Ref. [5].

where K_i increases (k_i decreases) with an increase in i. The bin width $\Delta k_i = |k_i - k_{i-1}|$ depends on i. Subsequently, $\widetilde{\phi}_{ilm}(\mathbf{r}_4)$ is generated by using Eq. (5.2) with energy $\widetilde{\varepsilon}_i$. Finally, $\widetilde{E}_i$ is expressed as Eq. (5.3) as shown in Fig. 8.

Similar to Ref. [5], we consider $N = 200$ setting $\hbar K_N = 6.0$ MeV/c ($E_N = 175$ keV) in Fig. 8. This is sufficient for deriving the muon momentum spectrum with a smooth function.

A. Fusion rate of the $dt\mu$ molecule

In our model, instead of Eq. (6.4) in Ref. [5], we can write the reaction rate to a continuum discretized state $(\alpha n)_{il}$,

$$(dt\mu)_{J=v=0} \to (\alpha n)_{il} + \mu + 17.6\,\mathrm{MeV}, \tag{5.5}$$

as follows:

$$r_{il} = v_{il}\left(\frac{\mu_{R_4}}{2\pi\hbar^2}\right)^2 \sum_{m,m_s}\int \left|T^{(4)}_{il,mm_s}\right|^2 \mathrm{d}\widetilde{\widetilde{\mathbf{K}}}_i, \tag{5.6}$$

where $v_{il} = \hbar\widetilde{K}_i/\mu_{R_4}$ is the $(\alpha n)_{il}$-μ relative velocity.

The sum of the transition rates

$$\lambda^{(4)}_{\mathrm{f}} = \sum_{il} r_{il} \tag{5.7}$$

is the fusion rate of the $(dt\mu)_{J=v=0}$ molecule using the T matrix based on channel $c = 4$ (cf. Eq. (6.5) in Ref. [5]). The contribution to $\lambda^{(4)}_{\mathrm{f}}$ from the final states $\widetilde{\phi}_{ilm}(\mathbf{r}_4)$ with $l \neq 2$ is negligible under the present dt-αn tensor coupling interaction.

The calculated fusion rates $\lambda^{(4)}_{\mathrm{f}}$ are presented in the final column of Table V for 20 sets of potentials listed in Table IV. $\lambda^{(4)}_{\mathrm{f}} = 1.1$–$1.2 \times 10^{12}\mathrm{s}^{-1}$ exhibits minimal dependence on the potential sets and agrees with the result ($1.15 \times 10^{12}\mathrm{s}^{-1}$) presented in Ref. [5]. Moreover, the fusion rates $\lambda^{(4)}_{\mathrm{f}}$ and $\lambda^{(5)}_{\mathrm{f}}$ under the same potential set yield almost the same values.

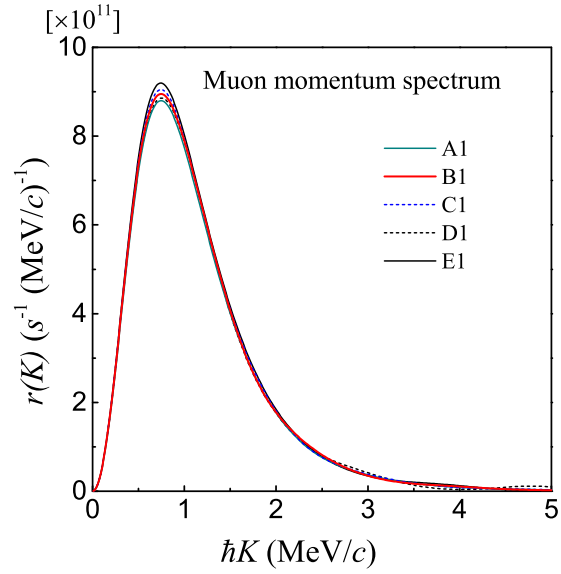

FIG. 9. Momentum spectrum $r(K)$ of the muon emitted by the μCF reaction (1.2), which are calculated with Eq. (5.8) using the potential Sets A1, B1, C1, D1, and E1 listed in Table IV.

B. Momentum and energy spectrum of the ejected muon

This subsection presents the muon momentum and energy spectra derived as continuous functions of K and the kinetic energy E, respectively, following Sec. VI B of Ref. [5]. The momentum spectra, $r(K)$, is obtained by smoothing r_{il} of Eq. (5.6) as

$$\lambda^{(4)}_{\mathrm{f}} = \sum_{il}\left(\frac{r_{il}}{\Delta K}\right)\Delta K \overset{\Delta K\to 0}{\longrightarrow} \int_0^{K_N} r(K)\,\mathrm{d}K, \tag{5.8}$$

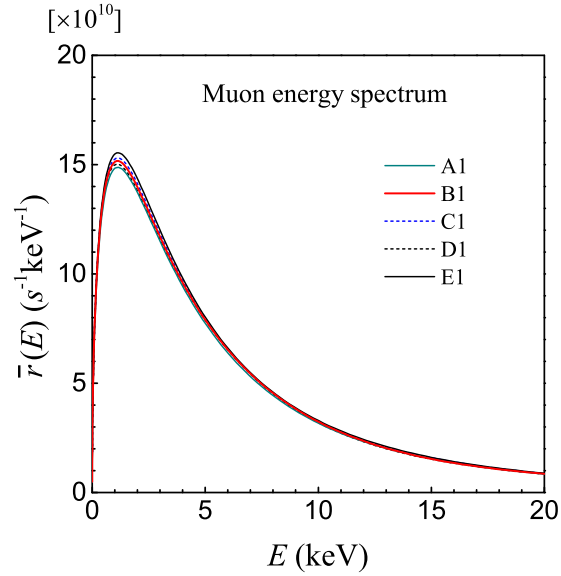

FIG. 10. Energy spectrum $\bar{r}(E)$ of the muon emitted by the μCF reaction (1.2), which is calculated with Eq. (5.9) using potential Sets A1, B1, C1, D1, and E1 listed in Table IV.

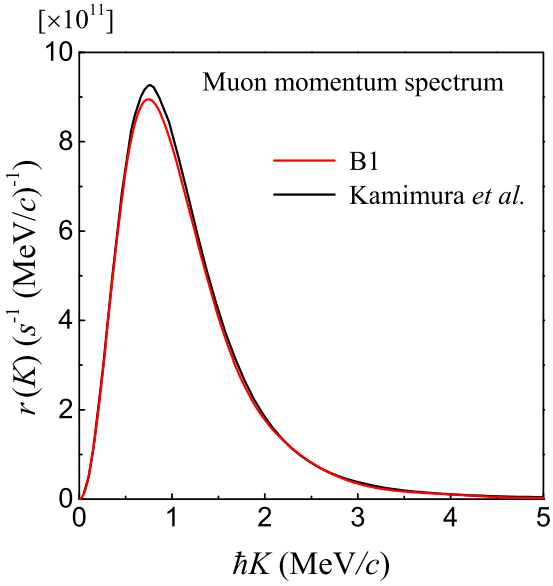

FIG. 11. Momentum spectrum $r(K)$ of the ejected muon (red line) calculated with the potential Set B1 in Fig. 9 in comparison to $r(K)$ given by Kamimura *et al.* in Fig. 14 of Ref. [5].

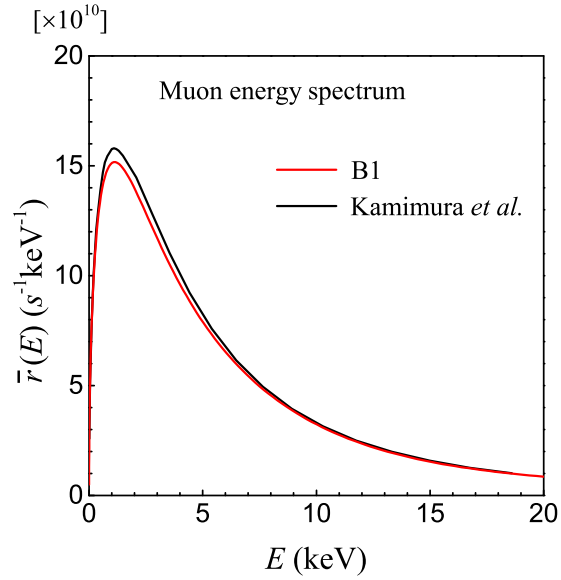

FIG. 12. Energy spectrum $\bar{r}(E)$ of the ejected muon (red line) calculated with the potential Set B1 in Fig. 10 in comparison to $\bar{r}(E)$ given by Kamimura *et al.* in Fig. 15 of Ref. [5].

where the present case $\Delta K = 0.03$ MeV is sufficiently small. The energy distribution, $\bar{r}(E)$, is derived as follows:

$$\bar{r}(E)\,\mathrm{d}E = r(K)\,\mathrm{d}K, \quad E = \hbar^2 K^2/2\mu_{\mathrm{R}_4}. \tag{5.9}$$

Figures 9 and 10 illustrate the muon momentum spectrum $r(K)$ and the energy spectrum $\bar{r}(E)$ calculated using the potential Sets A1, B1, C1, D1, and E1 (Table IV). The five lines are close to each other in both the figures. This demonstrates that our results are potentially independent of each other. Further, we verified that the figures obtained using potentials A3–E3 are similar to Figs. 9 and 10.

In Figs. 11 and 12, we compare our results for $r(K)$ and $\bar{r}(E)$ (red lines using Set B1) with the results in Ref. [5] (black lines) taken from Figs. 14 and 15 using Eqs. (6.9) and (6.11), respectively. Our results agree well with those reported in Ref. [5]. The use of any other potential set also reproduces the result of Ref. [5] as is understood from Figs. 9 and 11.

In Table VI, the peak and average energies of the muon energy spectrum $\bar{r}(E)$ and those reported in Ref. [5] are compared. The peak energy is located at $E \approx 1.1$ keV both in our T-matrix model and in Ref. [5]. The average energy of 8.9 keV (Set B1) is also consistent with the result (9.5 keV) from Ref. [5]. This large average energy is caused by the long high-energy tail of the energy spectrum as evident in Fig. 12. Therefore, it can be concluded that muons with peak energy of ≈1 keV and the average energy of ≈10 keV are emitted by $dt\mu$ fusion, which is the same as in Ref. [5]. These results will be helpful to the ongoing experimental project for generate an ultraslow negative muon beam using μCF for various applications.

TABLE VI. Property of the muon energy spectrum $\bar{r}(E)$ by the present result with the use of potential Set B1 (Fig. 12). The case of $\bar{r}(E)$ given by Ref. [5] is also listed for comparison.

Muon energy spectrum	Peak energy (keV)	Average energy (keV)	Peak strength $(\mathrm{s\,keV})^{-1}$
Present, $\bar{r}(E)$ with B1	1.1	8.9	1.54×10^{11}
$\bar{r}(E)$ (Ref. [5])	1.1	9.5	1.60×10^{11}

VI. CONCLUSION

Recently, a comprehensive study of the μCF reaction (1.2) was performed in Ref. [5] by solving two coupled channel (CC) Schrödinger equations for the reactions (1.1) and (1.2). In the present study, we have proposed a considerably more tractable T-matrix model to simulate the CC model [5] by considering scenarios (i) –(v):

(i) We reproduced the low-energy cross sections of reaction (1.1) by using an optical-potential (OP) model (Fig. 2 and Table I). The effect of the α-n channel is considered to be included using the imaginary part of the optical potential.

(ii) The exact T matrix for the reaction (1.1) was approximated by replacing the exact CC wave function with the OP-model wave function obtained in i). The cross section of the reaction (1.1) was expressed by the simple closed form (3.10) based on our model and reproduced the observed cross section by properly selecting the dt-αn coupling potential (Fig. 5 and Table IV).

(iii) We calculated the $(dt\mu)_{J=v=0}$ molecular wave function including the OP-model d-t potential determined in (i).

(iv) We approximated the full T matrix in Ref. [5] for the reaction (1.2) as follows: We replaced the CC wave function for this reaction with the muonic $(dt\mu)_{J=v=0}$ wave function obtained in (iii).

(v) Using the approximated T matrix in (iv), we calculated the reaction rates to the α-μ continuum and the bound states, fusion rates of reaction (1.2), α-μ sticking probability, and momentum and energy spectra of muons emitted by reaction (1.2). Most of the results obtained in Ref. [5] were well reproduced.

All the calculated results were insensitive to 20 sets of d-t potential and dt-αn coupling potential. In practical calculations, the use of only a few sets is sufficient.

Thus, the proposed tractable T-matrix model was constructed, such that it reproduced most of the results obtained in Ref. [5]. This model is applicable to other μCF systems such as $(dd\mu)$, $(tt\mu)$, $(dt\mu)^*$, and $(dd\mu)^*$.

ACKNOWLEDGMENTS

The authors would like to thank Prof. Y. Kino and Dr. T. Yamashita for their valuable discussions in the study. This work is supported by the Grant-in-Aid for Scientific Research on Innovative Areas, "Toward new frontiers: Encounter and synergy of state-of-the-art astronomical detectors and exotic quantum beams", JSPS KAKENHI Grant No. JP18H05461. This work is also supported by Natural Science Foundation of Jiangsu Province (Grant No. BK20220122), and National Natural Science Foundation of China (Grant No. 12233002).

[1] W. H. Breunlich, P. Kammel, J. S. Cohen, and M. Leon, Annu. Rev. Nucl. Part. Sci. **39**, 311 (1989).
[2] L. I. Ponomarev, Contemp. Phys. **31**, 219 (1990).
[3] K. Nagamine and M. Kamimura, Adv. Nucl. Phys. **24**, 151 (1998).
[4] P. Froelich, Adv. Phys. **41**, 405 (1992).
[5] M. Kamimura, Y. Kino, and T. Yamashita, Phys. Rev. C **107**, 034607 (2023).
[6] T. Yamashita, K. Okutsu, Y. Kino, S. Okada, and M. Sato, Sci. Rep. **12**, 6393 (2022).
[7] M. Kamimura, Y. Kino, and T. Yamashita (private communication).
[8] B. A. Lippmann and J. Schwinger, Phys. Rev. **79**, 469 (1950).
[9] M. Kamimura, AIP Conf. Pro. **181**, 330 (1989).
[10] P. D. Serpico, S. Esposito, F. Iocco, G. Mangano, G. Miele, and O. Pisanti, J. Cosmol. Astropart. Phys. **2004**, 010 (2004).
[11] M. Kamimura, Phys. Rev. A **38**, 621 (1988).
[12] H. Kameyama, M. Kamimura, and Y. Fukushima, Phys. Rev. C **40**, 974 (1989).
[13] E. Hiyama, Y. Kino, and M. Kamimura, Prog. Part. Nucl. Phys. **51**, 223 (2003).
[14] M. Kamimura, Y. Kino, and T. Yamashita, arXiv:2112.08399v1 (2021), an earlier version of Ref. [5].
[15] M. Kamimura, M. Yahiro, Y. Iseri, Y. Sakuragi, H. Kameyama, and M. Kawai, Prog. Theor. Phys. Suppl. **89**, 1 (1986).
[16] N. Austern, Y. Iseri, M. Kamimura, M. Kawai, G. Rawitscher, and M. Yahiro, Phys. Rep. **154**, 125 (1987).
[17] M. Yahiro, K. Ogata, T. Matsumoto, and K. Minomo, Prog. Theor. Exp. Phys. **2012**, 1A206 (2012).
[18] L. N. Bogdanova, V. E. Markushin, V. S. Melezhik, and L. I. Ponomarev, Yad. Fiz. **50**, 1365 (1989) [Sov. J. Nucl. Phys. **50**, 848 (1989)].
[19] M. C. Struensee, G. M. Hale, R. T. Pack, and J. S. Cohen, Phys. Rev. A **37**, 340 (1988).
[20] K. Szalewicz, B. Jeziorski, A. Scrinzi, X. Zhao, R. Moszynski, W. Kolos, P. Froelich, H. J. Monkhorst, and A. Velenik, Phys. Rev. A **42**, 3768 (1990).
[21] G. M. Hale, M. B. Chadwick, J. S. Cohen, and C.-Y. Hu, Hyperfine Interact. **82**, 213 (1993).
[22] C. Y. Hu, G. M. Hale, and J. S. Cohen, Phys. Rev. A **49**, 4481 (1994).
[23] J. S. Cohen, G. M. Hale, and C. Y. Hu, Hyperfine Interact. **101-102**, 349 (1996).
[24] B. Jeziorski, K. Szalewicz, A. Scrinzi, X. Zhao, R. Moszynski, W. Kolos, and A. Velenik, Phys. Rev. A **43**, 1640 (1991).